Emission of terahertz radiation from dual grating gate plasmon-resonant emitters fabricated with InGaP/InGaAs/GaAs material systems

2008 J. Phys.: Condens. Matter 20 384206

(http://iopscience.iop.org/0953-8984/20/38/384206)

J. Phys.: Condens. Matter **20** (2008) 384206 (11pp) doi:10.1088/0953-8984/20/38/384206

Emission of terahertz radiation from dual grating gate plasmon-resonant emitters fabricated with InGaP/InGaAs/GaAs material systems

T Otsuji[1], Y M Meziani[1], T Nishimura[1], T Suemitsu[1], W Knap[1,2], E Sano[3], T Asano[4] and V V Popov[5]

[1] Research Institute of Electrical Communication, Tohoku University, Sendai 980-8577, Japan
[2] GES-UMR5650, Universite Montpellier 2 and CNRS, Montpellier 34095, France
[3] Research Center for Integrated Quantum Electronics, Hokkaido University, Sapporo 060-8628, Japan
[4] Department of Electronics, Faculty of Information Science and Electrical Engineering, Kyushu University, Fukuoka 819-0395, Japan
[5] Institute of Radio Engineering and Electronics (Saratov Branch), Saratov 410019, Russia

E-mail: otsuji@riec.tohoku.ac.jp

Received 2 May 2008, in final form 8 June 2008
Published 21 August 2008
Online at stacks.iop.org/JPhysCM/20/384206

Abstract
This paper reviews recent advances in our original 2D-plasmon-resonant terahertz emitters. The structure is based on a high-electron-mobility transistor and featured with doubly interdigitated grating gates. The dual grating gates can alternately modulate the 2D electron densities to periodically distribute the plasmonic cavities along the channel, acting as an antenna. The device can emit broadband terahertz radiation even at room temperature from self-oscillating 2D plasmons under the DC-biased conditions. When the device is subjected to laser illumination, photo-generated carriers stimulate the plasma oscillation, resulting in enhancement of the emission. The first sample was fabricated with standard GaAs-based heterostructure material systems, achieving room temperature terahertz emission. The second sample was fabricated in a double-decked HEMT structure in which the grating gate metal layer was replaced with the semiconducting upper-deck 2D electron layer, resulting in enhancement of emission by one order of magnitude.

1. Introduction

Development of compact, tunable and coherent sources operating at terahertz frequencies is one of the hottest issues of the modern terahertz (THz) electronics [1]. Two-dimensional (2D) plasmons in submicron transistors have attracted much attention due to their nature of promoting emission of electromagnetic radiation. The frequency of plasma oscillations in low-dimensional systems increases on lowering the dimension and can reach frequencies in the THz region. Therefore different devices/structures of micron and submicron size supporting low-dimensional plasmons were intensively studied as possible candidates for solid-state far-infrared (FIR)/THz sources [1–15]. Mechanisms of plasma wave excitation/emission can be divided (by convention) into two types—(i) incoherent and (ii) coherent type. The first is related to thermal excitation of broadband nonresonant plasmons by hot electrons [2–7]. The second is related either to the plasma wave instability mechanisms like Dyakonov–Shur [8] and/or to the electron transit-time effect [16], where coherent plasmons can be excited either by hot electrons or also by optical phonon emission under near ballistic electron motion [17].

Historically, first experimental observations of THz emission from 2D plasmons involved the first incoherent

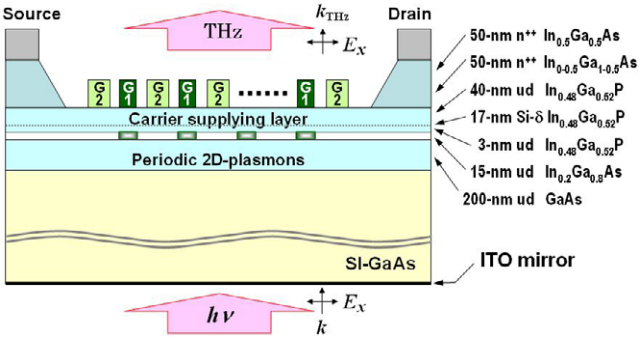

Figure 1. Device cross-section for typical GaAs-based heterostructure material systems. k, the wavevectors of irradiated photons; E_x, the electric field (linear polarization); k_{THz}, the wavevector of electromagnetic radiation. Reprinted from [26]. Copyright 2007, with permission from Elsevier.

mechanism: the radiative decay of hot plasmons. Many authors proposed the radiative decay of grating-coupled 2D plasmons in semiconductor heterostructures as one of the most promising candidates for tunable solid-state FIR/THz sources [2–8, 12]. THz emission from hot 2D plasmons has been observed from selectively doped GaAs/AlGaAs heterostructures as well as Si metal–oxide–semiconductor field effect transistors. In spite of its potential applications, only cryogenic-temperature (4 K) emitters were reported. THz emission from coherent plasmon excitations at both cryogenic and room temperatures were also studied [9–11, 18–21]. Room temperature THz emission interpreted in terms of Dyakonov–Shur instability was observed from nanometer size GaInAs and GaN/AlGaN high-electron-mobility transistors (HEMTs) [9–11]. Room temperature optically excited resonant plasmon modes were also observed in double grating gate structures [22–29].

This paper reviews recent advances in our original 2D-plasmon-resonant terahertz emitters [22–31]. The structure is based on an HEMT and featured with doubly interdigitated grating gates. The dual grating gates can alternately modulate the 2D electron densities to periodically distribute the plasmonic cavities along the channel, acting as an antenna. The device can emit broadband terahertz radiation even at room temperature from self-oscillating 2D plasmons under DC-biased conditions. When the device is subjected to laser illumination, photo-generated carriers stimulate the plasma oscillation, resulting in enhancement of the emission. The first sample is designed and fabricated with standard GaAs-based heterostructure material systems. The second sample is fabricated in a double-decked HEMT structure in which the grating gate metal layer is replaced with the semiconducting upper-deck 2D electron layer to enhance the radiation power.

2. Device structure and operation

Figure 1 illustrates the cross-section of the plasmon-resonant emitter [30]. The device structure is based on an HEMT and incorporates (i) doubly interdigitated grating gates (G1 and G2) that periodically localize the 2D plasmon in stripes of the order of 100 nm with a micron-to-submicron interval and (ii) a vertical cavity structure in between the top grating plane and a terahertz mirror at the backside. The structure (i) works as a terahertz antenna and (ii) works as an amplifier. The terahertz mirror is to be a transparent metal like indium titanium oxide (ITO) when the device works in an optical excitation mode so as to excite the plasmons by optical two-photon irradiation from outside the back surface.

Suppose that the grating gates have geometry with 300 nm G1 fingers and 100 nm G2 fingers to be aligned alternately with a space of 100 nm and that an appropriately high 2D electronic charge ($\sim 10^{12}$ cm^{-2}) is induced in the plasmon cavities under G1 while the regions under G2 are weakly charged (10^{10}–10^{11} cm^{-2}). Figure 2 depicts numerically simulated typical 2D electron density/velocity distributions based on self-consistent drift-diffusion Poisson equations. A standard DC drain-to-source bias V_{DS} of 50 mV/(grating period), and the gate biases V_{G1} and V_{G2} of V_{th} + 2.2 V and V_{th} + 0.2 V, are assumed, where V_{th} is the threshold voltage. As is seen in figure 2, a strong electric field (1–10 kV cm^{-1}) arises at the plasmon cavity boundaries. When the DC drain-to-source

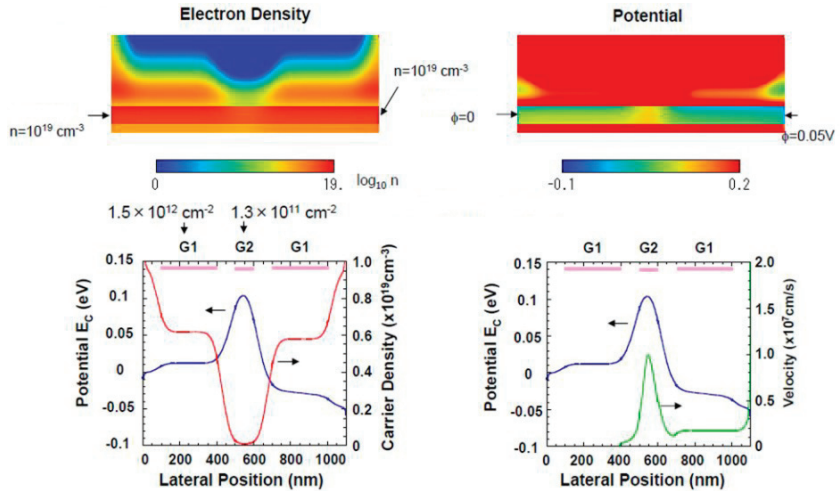

Figure 2. Electron density/velocity distributions in a unit of the 2D plasmon grating cavities. $V_{DS} = 50$ mV/(grating period), $V_{G1} = V_{th} + 2.2$ V, $V_{G2} = V_{th} + 0.2$ V.

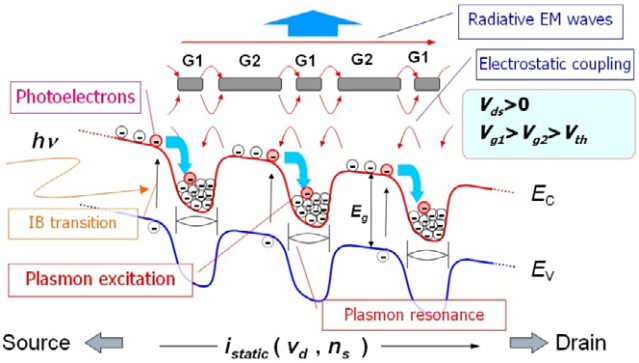

Figure 3. Schematic band diagram and operation mechanism.

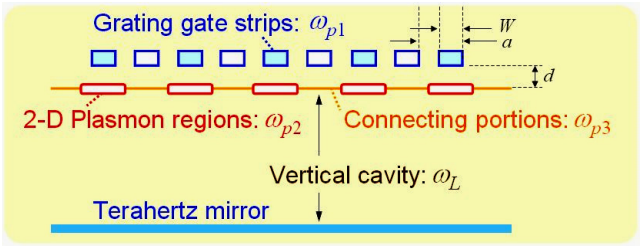

Figure 4. Characteristic frequencies. Reproduced from [30]. Copyright 2008 with permission from the Optical Society of America.

bias V_{DS} is applied, 2D electrons are accelerated to produce a constant drain-to-source current I_{DS}. Due to such a distributed plasmonic cavity system with periodic 2D electron-density modulation, the DC current flow may excite the plasma waves in each plasmon cavity. As shown in figure 3, asymmetric cavity boundaries make plasma wave reflections as well as abrupt change in the density and the drift velocity of electrons, which may cause the current-driven plasmon instability [8, 12] leading to excitation of coherent resonant plasmons. Thermally excited hot electrons also may excite incoherent plasmons. The grating gates act also as terahertz antenna that converts non-radiative longitudinal plasmon modes to radiative transverse electromagnetic modes.

When the device is photoexcited by laser irradiation, photoelectrons are predominantly generated in the weakly charged regions with many unoccupied electronic states under G2 and then are injected to the plasmon cavities under G1. If a specific drain-to-source bias is applied to promote a uniform slope along the source-to-drain direction on the energy band in the regions under G2 as shown in figure 3, photoelectrons under G2 are unidirectionally injected to one side of the adjacent plasmon cavity. This may also excite the plasmons under an asymmetric cavity boundary [32, 33]. It is noted that the laser irradiation may excite the plasmon not only in the regions under G1 but also in the regions under G2 if the cavity size and carrier density of the regions under G2 also satisfy the resonant conditions.

Once the terahertz electromagnetic waves are produced from the seed of plasma waves, downward-propagating electromagnetic waves are reflected at the mirror back to the plasmon region so that the reflected waves can directly excite the plasmon again according to the Drude optical conductivity and intersubband transition process [30]. When the plasmon-resonant frequency satisfies the standing wave condition of the vertical cavity, the terahertz electromagnetic radiation will reinforce the plasmon resonance in a recursive manner. Therefore, the vertical cavity may work as an amplifier if the gain exceeds the cavity loss. The quality factor of the vertical cavity is relatively low, as is simulated in [30], since the 2D plasmon grating plane of one side of the cavity boundary must have a certain transmittance for emission of radiation. Thus, the cavity serves a broadband function.

3. Design and fabrication

3.1. Characteristic parameters and design scheme

Field emission properties of the dual grating gate plasmon-resonant emitters are characterized by the structure dependent key parameters shown in figure 4 [28]. The primary parameter that initiates the plasmon resonance is ω_{p2}, which is the plasma frequency, i.e. plasmon characteristic frequency, of the periodically confined *gated* plasmon cavities. Each cavity is connected by the connecting portion whose carrier density must be controlled to be far apart from that in the plasmon cavity to make a good plasmon confinement. Thus, this connecting portion has its characteristic frequency ω_{p3}. The grating gate also has its own plasma frequency ω_{p1}. Note that ω_{p2} and ω_{p3} for the *gated* plasmon cavities and connecting portions obey the linear dispersion law, while ω_{p1} for the *ungated* gate gratings is proportional to the square root of the wavevector [8, 12, 30]. All three parameters are mainly determined by their cavity length, W, the distance between layers, d, and carrier density, and perturbed by their periodicity, a, or the filling parameter, $f = W/a$[12]. The final parameter, denoted by ω_L, corresponds to the vertical cavity resonance.

According to the operating frequency band, the grating geometry (single plasmon cavity length and periodicity) is designed to be fixed and ω_{p1}, ω_{p3} as well as ω_L are optimally designed. For actual device operation, ω_{p2} is a given parameter, which is first tuned by the gate bias at a specific value to obtain a desired resonance frequency. As a fundamental design criterion to obtaining high quantum efficiency, the ω_{p1} and ω_L values are to be matched to the ω_{p2} value while ω_{p3} is far away from them. Once the device dimensions and material systems are designed, ω_{p1} and ω_L become fixed parameters. ω_{p3} for the connecting portion, on the other hand, is controllable (by V_{g2}) so that one can set it far higher or lower than ω_{p2} by making the connecting portion metallic or dielectric. When the grating gate is made with metals like standard HEMTs, ω_{p1} becomes higher by orders of magnitude than ω_{p2}, resulting in degrading the emission power/efficiency [30, 31]. To prevent this, a semiconducting material, in particular, 2DEG grating gate made from the upper deck of a double-decked HEMT, is superior, which is demonstrated in section 5.

The plasma wave behavior of the 2D electron system (2DES) is described by the extended Dyakonov–Shur model [8, 30]. Under the gradual channel approximation, the local electron density n and velocity v of the plasma fluid are

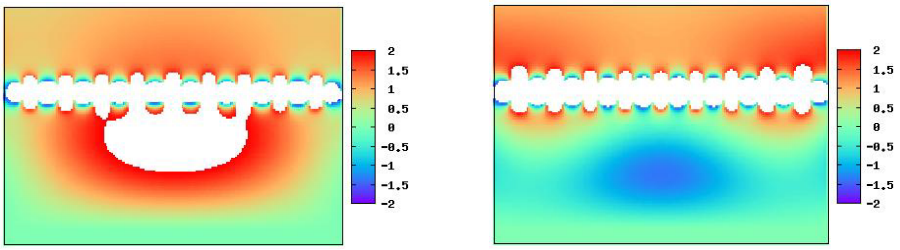

(a) (b)

Figure 5. Simulated instantaneous electric field (E_x) distributions under a constant sinusoidal plasmon excitation at (a) 3.4 THz and (b) 5.1 THz. The intensity scale on the indicator is in arbitrary units. Reproduced from [30]. Copyright 2008 with permission from the Optical Society of America.

formulated by the hydrodynamic equations

$$m_e\left(\frac{\partial \mathbf{v}}{\partial t} + (\mathbf{v}\cdot\nabla)\mathbf{v}\right) = -e\nabla U - m_e\frac{\mathbf{v}}{\tau}, \quad (1)$$

$$\frac{\partial n}{\partial t} + \nabla(n\mathbf{v}) = \frac{\partial U}{\partial t} + \nabla(U\mathbf{v}) = 0, \quad (2)$$

where m_e the electron effective mass, e the electronic charge, U the gate-to-channel potential and τ the plasmon relaxation time. Their time-evolved response to the terahertz excitation is numerically analyzed using the finite-differential time-domain (FDTD) method. The plasma waves themselves are the coherent electronic polarization so that they should produce local displacement AC current. Thus, it is input to the Maxwell's FDTD simulator as a current source to analyze the electromagnetic field dynamics.

Figure 5 shows the typical instantaneous cross-sectional distribution of the electric field intensity along the x (source to drain) direction under a constant sinusoidal plasmon excitation at (a) a tuned frequency of 3.4 THz and (b) a detuned frequency of 5.1 THz. The device model is based on the HEMT shown in figure 1, accommodating nine periods of the dual grating gates. The gate finger lengths, L_{G1} and L_{G2}, of 0.2 and 0.9 μm with 0.1 μm spacing are assumed. The characteristic frequencies ω_{p1} and ω_L are set at 3.4 THz. The primary parameter ω_{p2} is set at the excitation frequency (3.4 THz for (a) and 5.1 THz for (b)). All the plasmon cavities are excited in phase. One can see in figure 5(a) an in-phase oscillation between outside air (upper portion) and inside the cavity since the vertical cavity length is set at a quarter wavelength of the fundamental mode. The white colored area shows very high intensity of over the range. Under a detuned condition of 5.1 THz excitation, on the other hand, antiphase oscillation is seen as is expected. The radiation power almost remains at the level of that for the tuned condition. For both cases, the periodic longitudinal polarization in the plasmon grating plane is satisfactorily converted to the transverse monotonic electric field outside the device (upper portion in figure 5). The results clearly show the standing wave oscillation inside the cavity and forward-propagating quasi-transverse electromagnetic (TEM) waves outside in air.

In order to examine how the double gate grating and vertical cavity structures contribute to the field emission properties, artificial structures without a double gate grating and/or terahertz mirror are prepared, and their impulse responses compared to that of the original structure by using Maxwell's FDTD simulator. All the characteristic parameters were fixed at the nominal values ($\omega_{p1} = \omega_{p2} = \omega_L =$ 3.4 THz). Each plasmon cavity was excited with an impulsive current source simultaneously. Simulated temporal responses of the electric field (x component) at the central two points (4 μm beyond the gate surface and 4 μm beneath the plasmon surface) were Fourier transformed to obtain entire frequency spectra. Figure 6 plots the results. For the structures without gate gratings, neither *gated* plasmon modes nor the Smith–Purcell effect is produced, resulting in no obvious field enhancement over the frequency range; a small dip below 1 THz is an unphysical error caused in the numerical process. The vertical cavity gives a resonance property and weakly enhances the radiation in narrow bands around the fundamental and second harmonic frequencies.

Incorporating the double gate grating, in contrast, produces extraordinary electromagnetic transmission; the electric field intensity drastically enhances over a broadband range. As a result, mode-conversion gain, from non-radiative plasmon mode to radiative mode, of up to 14 dB (a factor of 5) was successfully obtained in a wide frequency range from 600 GHz to 4 THz, corresponding to the fundamental plasmon resonance. One can see that the fundamental peak stays at around 1.8 THz in the outside air, which is rather lower than the original characteristic frequency of ω_{p2}. One possible reason for this would be the excitation of vertically coupled surface plasmon polaritons as is seen in the interfaces of metallic gratings [30]. It is noted that the wavelength under consideration is larger by two orders of magnitude than the feature size of the grating, which is thought to be a consequence of excitation of complex plasmon modes produced in the grating-bicoupled unique structure.

3.2. Device fabrication

The device was fabricated with InGaP/InGaAs/GaAs material systems in two structures: a standard single-heterostructure HEMT with metallic grating gates [22–24, 26–28] and a double-decked (DD) HEMT with semiconducting two-dimensional electron gas (2DEG) grating gates [25, 29].

3.2.1. Metallic grating gate device. The SEM (scanning electron microscopy) images for a typical sample are shown

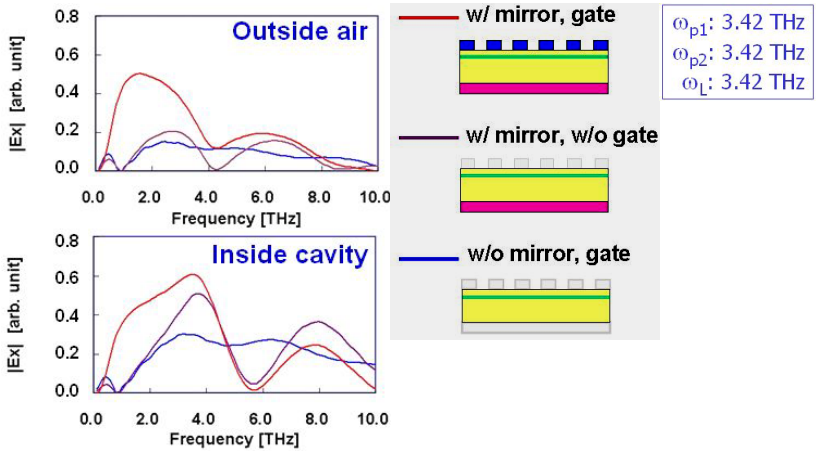

Figure 6. Simulated frequency responses for three different device structures to impulsive excitation at all the plasmon cavities. Electric fields (x component) at two points (inside the cavity and outside air) are calculated by using a Maxwell's FDTD simulator and their temporal profiles were Fourier transformed.

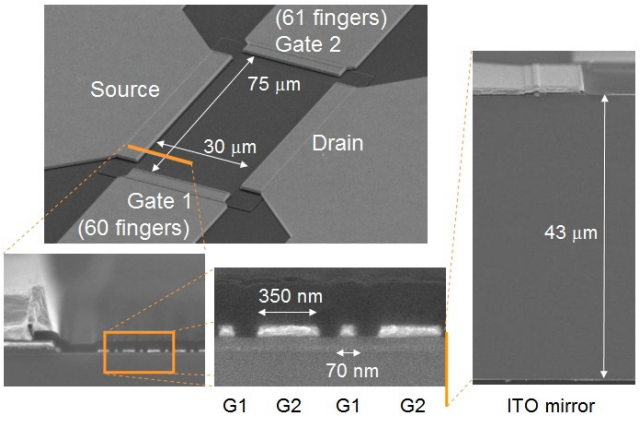

Figure 7. SEM images of a fabricated metal grating gate plasmon-resonant emitter. Reproduced from [25] with permission. © 2007 IEEE.

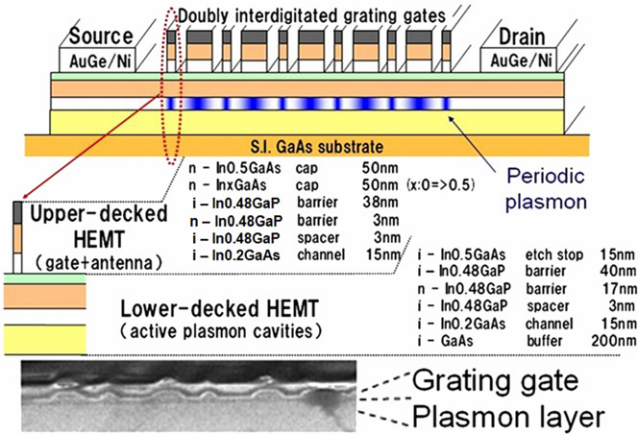

Figure 8. Cross-sectional structure and SEM image of a semiconducting grating gate plasmon-resonant emitter. Reproduced from [25] with permission. © 2007 IEEE.

in figure 7. The 2D plasmon layer is formed with a quantum well at the heterointerface between a 15 nm thick undoped InGaAs channel layer and a 60 nm thick, Si-δ-doped InGaP carrier-supplying layer. The grating gate was formed with 65 nm thick Ti/Au/Ti by a standard lift-off process. To cover operating frequencies from 1 to 10 THz, the grating geometry was designed with 350 nm G1 fingers and 100 nm G2 fingers to be aligned alternately with a space of 70 nm. The gate width is 75 μm for both G1 and G2. For comparison, another sample having a larger fraction of G1/G2 fingers (1800 nm/100 nm) was also fabricated. The number of gate fingers G1/G2 is 61/60 (38/37) for the sample having 300 nm (1800 nm) G1 fingers.

3.2.2. Semiconducting grating gate device. The device cross-sectional view and its SEM image are shown in figure 8 [25]. As described in section 3.1, the metal grating gates have a disadvantage that their characteristic frequencies do not match those for the periodic 2D plasmonic systems due to their extremely high conductivity. In the double-decked HEMT structure in this work, on the other hand, the upper-deck channel serves as the grating antenna and its structure is exactly the same as the lower channel. Therefore, more intensity in the emitted THz wave is expected. In this work, in order to produce the periodically localized 2DEG, the double-decked HEMT structure is employed. The upper-deck channel is then periodically etched as shown in figure 8 to form the uncapped region where the 2DEG concentration becomes lower than the capped region without any external gate bias. The HEMT structure consists of the InGaP/InGaAs/GaAs heterostructure with a selective doping in the InGaP layer. For the source/drain ohmic contacts, AuGe/Ni was lifted off and annealed after the upper-deck HEMT was selectively etched. The intrinsic device area has a geometry of 30 μm $\times$ 75 μm, where the grating pattern is replicated on the upper-deck HEMT layer. The grating consists of 80 nm lines and 350 nm lines aligned alternately with a spacing of 100 nm. The number of fingers is 60 (61) for the 80 nm (350 nm) grating.

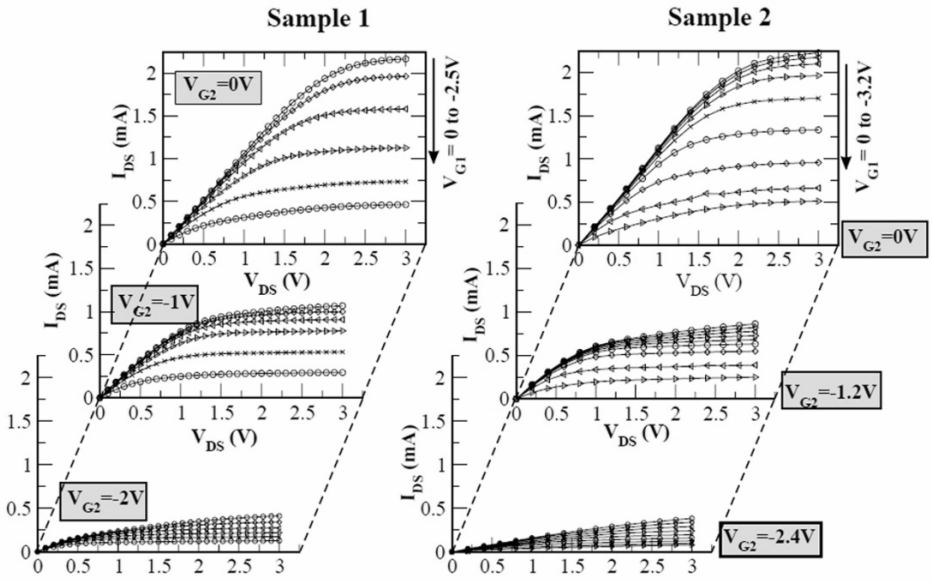

Figure 9. Measured I_{DS}–V_{DS} characteristics for metal grating gate devices under different V_{G1} and V_{G2} conditions. Grating gate geometry is (a) $L_{G1}/L_{G2} = 300$ nm/100 nm and (b) $L_{G1}/L_{G2} = 1800$ nm/100 nm. Reprinted from [26]. Copyright 2007, with permission from Elsevier.

4. Experimental results and discussion

4.1. DC characteristic

DC characteristics of the fabricated sample were first measured on a wafer. In the case of the metallic grating gate samples, as shown in figure 9 [26], the drain current I_{DS} shows FET-like dependence on the drain–source bias V_{DS}, and the 2D electron density in the channel is successfully modulated by the dual gate bias V_{G1} and V_{G2}. The threshold voltages V_{TH1} and V_{TH2} for V_{G1} and V_{G2} were identified at -2.5 and -3.5 V, respectively. The deeper V_{TH2} for the 100 nm gate is due to the short channel effect. The maximum value of an equivalent transconductance at $V_{DS} = 3.0$ V for G1 and G2: $\partial I_{DS}/\partial V_{G1,2}|_{max}$ are 14.3 and 12.6 mS mm^{-1} for sample 1 and 17.4 and 12.6 mS mm^{-1} for sample 2, respectively. Fitting these data to the drift-diffusion model gives the modulation of electron drift velocity and the 2D electron density $\{v_d, n_s\}$ ranging from $\{10^6$ cm s^{-1}, 10^{12} cm$^{-2}\}$ to $\{10^7$ cm s^{-1}, 10^{11} cm$^{-2}\}$.

In the case of the semiconducting grating gate samples in a double-decked HEMT structure, I_{DS} shows an FET-like pinch-off as shown in figure 10 [25], but unfortunately cannot be modulated by $V_{G1,2}$, which is attributed to the Fermi-level pinning presumably caused by undesirable surface states at the heterointerface between the lower and the upper decks. Note that the V_{DS} range is different from those of figure 9 because the double-decked HEMTs in this work suffer from large parasitic source and drain resistance.

4.2. Self-emission under DC bias

Fourier-transformed far-infrared spectroscopic (FTIR) measurements were carried out for these samples. The samples were placed in the source position of the vacuum cavity of the

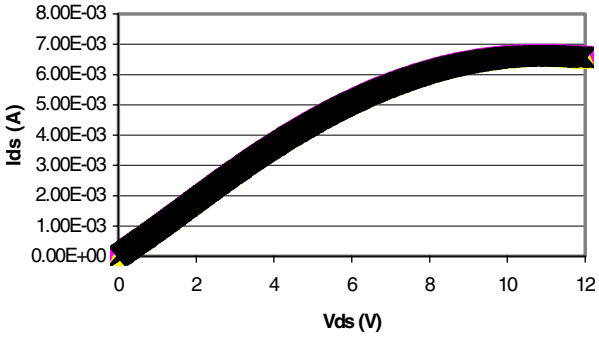

Figure 10. Measured I_{DS}–V_{DS} characteristics for a semiconducting grating gate sample. Grating gate geometry: $L_{G1}/L_{G2} = 150$ nm/1850 nm. Reproduced from [25] with permission. © 2007 IEEE.

FTIR. The radiation intensity was measured by an Si bolometer having a responsivity of 2.84×10^5 V W^{-1} and a noise-equivalent power (NEP) 1.16×10^{-13} W Hz$^{-1/2}$. The experimental procedure was the following: first we measured the background spectrum—the spectrum without any current flowing through the sample. This spectrum contained information on the 300 K blackbody emission modified by the spectral functions of all the elements inside the spectrometer. Then we measured the spectrum with current flowing through the sample.

FTIR measured emission spectra for metal grating gate samples having $L_{g1}/L_{g2} = 70$ nm/1850 nm and $L_{g1}/L_{g2} = 70$ nm/350 nm are shown in figures 11(a) and (b), respectively [29]. One can see relatively broad spectra starting from about 0.5 THz with maxima around 2.5 THz for the first sample (S1) and around 3.0 THz for the second one (S2); the grating geometry reflects the spectral profile. For both samples the emission dies off abruptly around 6.5 THz, which is thought to be due to the Reststrahlen band of optical phonon modes of the GaAs-based materials [28, 34].

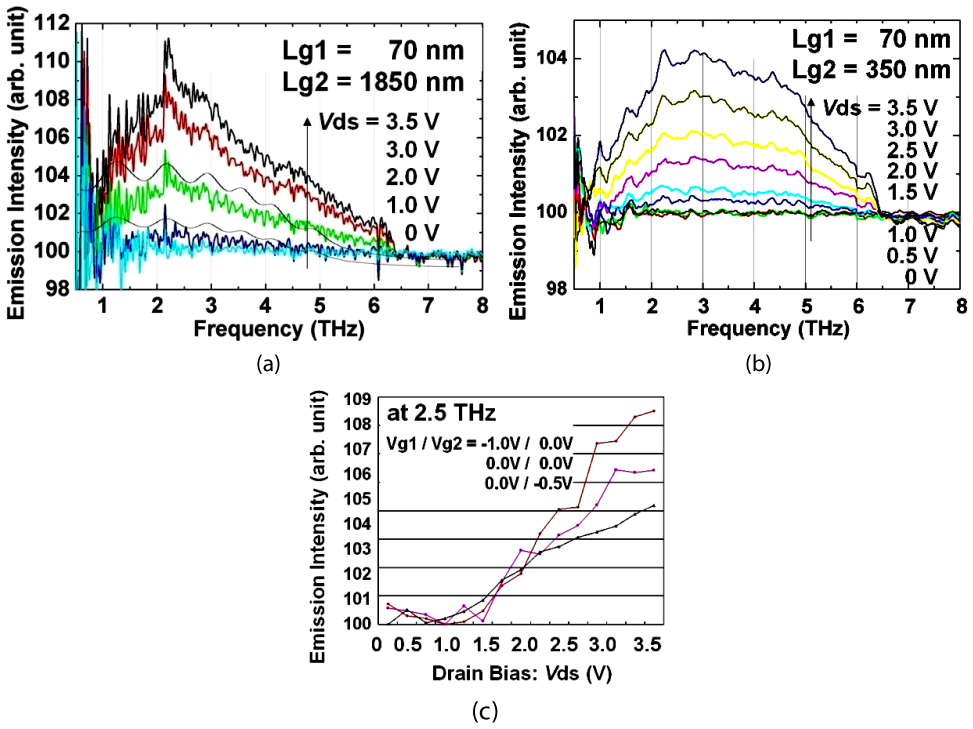

Figure 11. FTIR measured emission spectra for metal grating gate samples at room temperature. (a) $L_{g1}/L_{g2} = 70$ nm/1850 nm, (b) $L_{g1}/L_{g2} = 70$ nm/350 nm. The grating geometry reflects the emission spectra. (c) Emission intensity at 2.5 THz versus Vds for the sample with $L_{g1}/L_{g2} = 70$ nm/1850 nm, showing threshold behavior and super-linear (near quadratic) dependence on Vds. Two solid lines in (a) are calculated results for emissions from thermally excited plasmons at electronic temperatures of 310 and 320 K. Reproduced from [29] with permission. © 2008 IEEE.

The emission intensity versus V_{DS} is shown in figure 11(c). One can see that the emission intensity has a threshold property against V_{DS} and has a super-linear (nearly quadratic) dependence on V_{DS}. It is considered that the former property reflects on the coherent plasmons excited by the plasmon instability [8, 16], while the latter property is attributed to the emission caused by the thermally excited incoherent plasmons due to injection of drifting hot electrons into the plasmon cavities [28].

FTIR measured spectra for semiconducting grating gate samples having $L_{g1}/L_{g2} = 150$ nm/1850 nm are shown in figure 12. There is an intense emission power of the order of 1 μW for the DD-HEMTs at 300 K (one order of magnitude higher than that for MGG-HEMTs).

Dyakonov–Shur plasmon instability [8] and/or the Ryzhii–Satou–Shur transit-time instability [16] may take place at the cavity boundaries where the electron drift velocity (thus, 2DEG density) modulation predominantly occurs. Analytical calculation suggests that the instabilities are critically promoted near the drain side with low 2DEG densities when V_{DS} exceeds the pinch-off, resulting in the above-mentioned threshold property and enhancement of the emission at the low-frequency region around 2 THz. Since usually these coherent plasmon excitations are believed to have sharp spectral features, the observed spectral peaks may be attributed to these instability-driven emission.

The emission spectrum of thermally excited plasmons of the metallic grating gate structure was calculated based on a first-principles electromagnetic approach elaborated upon

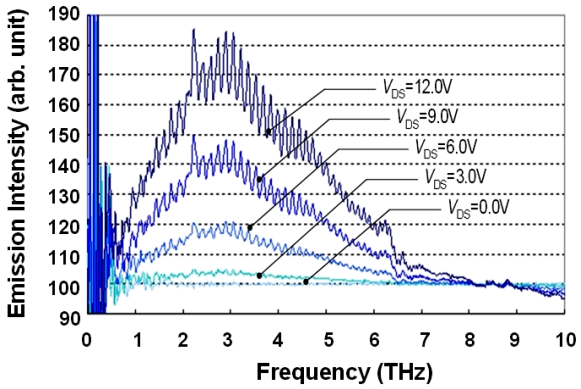

Figure 12. FTIR measured emission spectra for a semiconducting grating gate sample with $L_{g1}/L_{g2} = 150$ nm/1850 nm at room temperature. Reproduced from [29] with permission. © 2008 IEEE.

in [35, 36] where only a single metal grating in the structure is assumed, as is shown with solid lines in figure 11(a). In the calculated single period structure spectrum, the fundamental plasmon resonance appears at around 3 THz and the second one at about 4.5 THz. This may explain a pronounced bump around 5 THz in the high frequency shoulder in the short period structure experimental spectrum. The plasmon spectra in the actual double grating structure in question, of course, must be more complex compared to that in a single grating structure modeled numerically. In principle, two different sorts of plasmon cavities can be formed under the metal fingers of different width in the double grating structure.

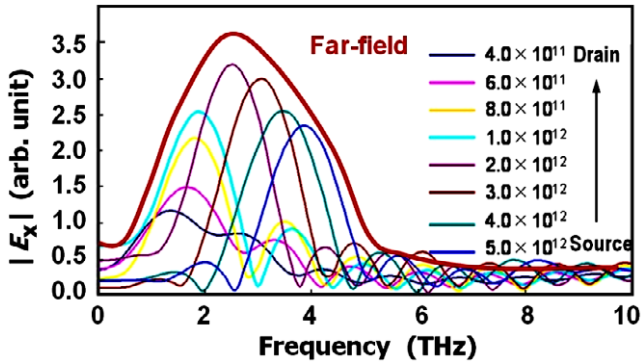

Figure 13. FDTD simulation for near-field and far-field emission spectra from a metal grating gate emitter when Vds is set at close to the pinch-off point. The plasmon cavities are formed under one grating gate with a 150 nm finger. The resultant 2DEG density distribution is depicted in the plot. Reproduced from [29] with permission. © 2008 IEEE.

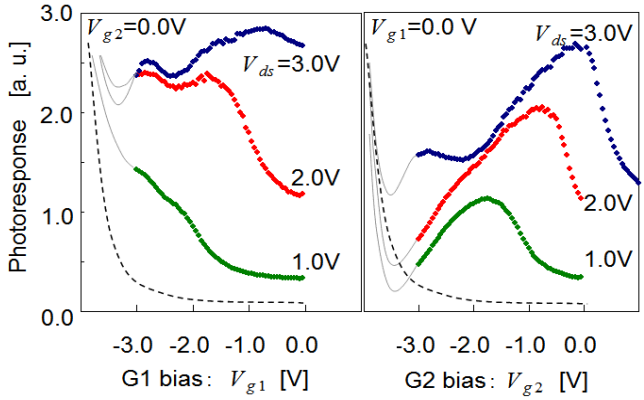

Figure 14. Measured photoresponse to single CW laser irradiation for a metal grating gate sample having a grating gate geometry of $L_{G1}/L_{G2} = 300$ nm/100 nm. The dotted line in the left plot is for a standard HEMT, showing a monotonic decrease with increase in gate bias. Reprinted from [26]. Copyright 2007, with permission from Elsevier.

Another fact of the V_{DS}-dependent 2DEG density slope must be considered to accurately explain the spectral profile, which is broader than that under a uniform 2DEG density condition. Near-field emission spectra at each section of the grating finger were simulated using a dedicated finite-differential time-domain simulator, in which the 2D plasmon dispersive/instability effects are modeled. Typical simulated results are shown in figure 13 [29]. Since the 2DEG densities in the plasmon cavities are dispersed from the source to the drain due to the applied V_{DS}, the peak emission frequency corresponding to the plasmon-resonant frequency shifts from the source to the drain. Such a spatial distribution on the near-field spectra are superposed at the far field, resulting in a spectral broadening [28].

From the above discussions, V_{DS}-dependent 2DEG density dispersion effects can significantly broaden the emission spectrum related to the coherent modes and the broadband part of the observed spectra can also contain THz emission originating from coherent plasma excitation mechanisms. Some coherent/resonant THz emission can be probably related to weak sharp features seen in the spectra—but clearly more studies are necessary to identify their origin.

4.3. Response to continuous-wave single laser irradiation

The device was irradiated from the backside with a lineally polarized 1550 nm band CW laser beam to measure its photoresponse at room temperature. A 1550 nm band tunable laser source with an average power of 2 mW was used. The polarization is set to be parallel to the channel direction. Actually, the photon energy of the irradiated laser is much lower than all the band gap energies of this material system. However, the electrons are weakly photoexcited at the InGaAs/GaAs heterointerface via multi-step processes due to the existence of deep trap centers [19]. The photoelectrons are injected to the channel immediately due to the strong gate-to-channel electric field.

When the plasma wave resonance is excited, the DC drain–source potential is modulated because of the nonlinear properties of the plasma fluid [31]. Therefore, the resonant intensity was measured by monitoring the DC modulation component ΔV_{DS} of the drain potential, which is called hereafter the photoresponse. The variation in ΔV_{DS} under irradiation was precisely lock-in amplified and detected at a chopping frequency of 1.29 kHz. At the same time, the terahertz radiation was detected using a 4.2 K cooled silicon bolometer with a filter pass band from 0.6 to 3.5 THz.

Typical results for the V_{G1} and V_{G2} dependence of the photoresponses of a metal grating gate sample ($L_{G1}/L_{G2} =$ 300 nm/100 nm) for different V_{DS} conditions are shown in figure 14 [26]. The device exhibited a marked photoresponse with relatively sharp peaks on its V_{G2} dependence and with broad peaks on its V_{G1} dependence. For V_{G2} dependence, when $V_{DS} = 1.0$ V, the photoresponse exhibited a clear single peak at $V_{G2} = -1.9$ V. According to the Dyakonov–Shur model [32] this photoresponse peak at the lowest gate bias is interpreted as the fundamental plasmon resonance. With increasing V_{DS} up to 3.0 V, the single peak becomes steeper and shifts to a higher V_{G2} point at around 0 V while the secondary peak grows at a lower V_{G2} point at -3.0 V, corresponding to the third harmonic plasmon resonance. Similarly, for V_{G1} dependence, when V_{DS} increases from 1.0 to 3.0 V, weak double dips on the background slope at $V_{DS} = 1.0$ V grow to clear double peaks at $V_{G1} = -0.8$ and -2.8 V.

The results are completely different from that for standard HEMT devices having a single gate finger fabricated on the same wafer showing monotonic dependence on the gate bias (plotted with a broken line in figure 14). Theoretical investigations in [12] and [37] suggest that the plasmon instability is promoted when electrons have a very high drift velocity of around 4×10^7 cm s^{-1} (equivalent plasma wave Mach number of around 0.5). Carrier dynamics under weakly photoexcited conditions in our device are simulated based on an extended drift-diffusion model [38]. The result indicates that the injection of photoelectrons from a weakly charged 2DEG to the adjacent deeply charged 2DEG (plasmon cavity) is performed in a quasi-ballistic manner so that the above-mentioned instability condition is obtainable.

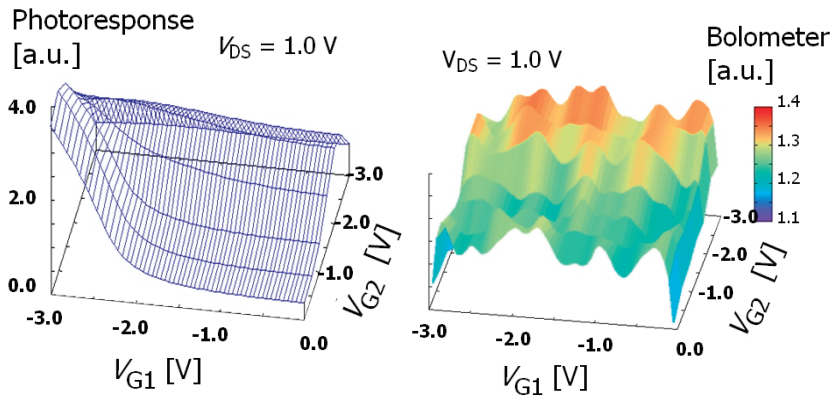

Figure 15. (a) Photoresponse and (b) 4 K cooled Si bolometer signal at $V_{DS} = 1.0$ V for a metal grating gate sample having a grating gate geometry of $L_{G1}/L_{G2} = 300$ nm/100 nm. Reprinted from [26]. Copyright 2007, with permission from Elsevier.

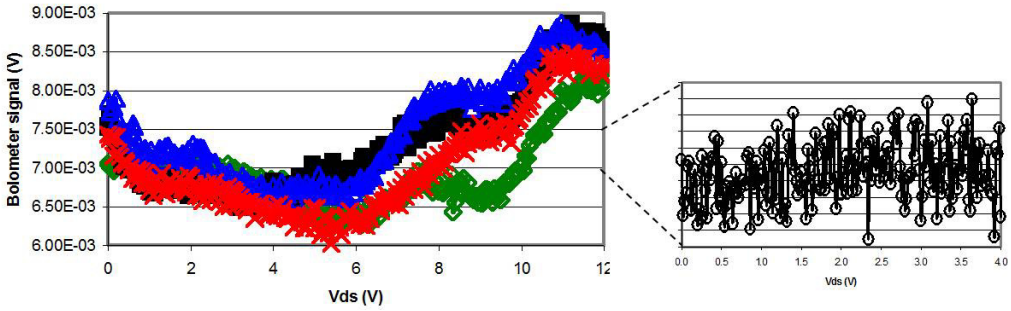

Figure 16. Left: bolometer detection of emission from a semiconducting grating gate sample with $L_{g1}/L_{g2} = 150$ nm/1850 nm at room temperature as a function of V_{DS}. Measurement took place four times. Bolometer signal increases rapidly at $V_{DS} > 6$ V (higher than the pinch-off), which is clear evidence of the THz-wave emission. Right: the result from a metal grating gate sample with $L_{g1}/L_{g2} = 75$ nm/350 nm for comparison. Reproduced from [25] with permission. © 2007 IEEE.

Focused on a simplest case at $V_{DS} = 1.0$ V, terahertz emission from the device was measured by using a 4 K cooled Si bolometer. At the same time, the device photoresponse was also measured. The measured results are plotted onto the V_{G1}–V_{G2} space as shown in figures 15(a) and (b) [26]. The photoresponse in figure 15(a) exhibits local maxima at $V_{G2} \approx -2.0$ V along the V_{G1} axis. In such a region, the bolometer shows clear enhancement of the signal. The observed signal is low and noisy due to atmospheric vapor absorption between the sample and the bolometer. According to well recognized responsivity of the order of 10^5 to 10^6 V W^{-1} for the Si composite bolometer used in this experiment (not calibrated) and atmospheric vapor absorption along with a 20 cm propagation from the device to the bolometer, the emission power is roughly estimated to be 0.1 μW from a single device. When $V_{G1} = -3$ V and $V_{G2} = 0$ V, in contrast, the photoresponse shows an increase but the bolometer does not detect the radiation. In this case, the photoresponse shows a nonresonant detection near to the threshold voltage. This phenomenon is well known as a space-charge effect of photoconductivity [39, 40]. Analytical calculation [8, 32] indicates that the emission at a frequency around 1.3–1.8 THz should occur when $V_{G2} \approx -2.5$ V and $V_{G1} = 0$ V for this sample, supporting the measured results.

The result of the bolometric measurement for a semiconducting grating gate sample is shown in figure 16 as a function of V_{DS}^{25}. The V_{DS} increases to the knee voltage from which the transistor is operated in the saturation region. The bolometer signal starts increasing at around 6 V and two clear peaks are observed at 8 and 11 V. These features were observed with good reproducibility, as shown in figure 16. Compared with the results for the metal grating gate sample, remarkable enhancement in emission intensity by one order of magnitude was obtained. Note that the V_{DS} range is larger than that for metal grating gate samples because the double-decked HEMTs in this work suffer from large parasitic source and drain resistance as mentioned in section 4.1. Nevertheless, the double-decked device exhibits more drastic change in the bolometer signal with increasing V_{DS}. This result supports the idea of a low-conductive gate stack to enhance the THz radiation efficiency [30, 31], and therefore indicates that the proposed double-decked HEMT structure is a promising candidate to realize solid-state THz-wave emitters with high power and large efficiency.

It is inferred, from such a phenomenological coincidence, that the marked photoresponse of this work is attributed to the plasmon excitation due to the injection of photoelectrons accelerated by the strong electric field arising at the plasmon cavity boundaries, leading to self-oscillation of emission of terahertz electromagnetic radiation. Significant improvement on the plasmon resonance is owing to the original device structure.

5. Conclusions

Recent advances in our original 2D-plasmon-resonant terahertz emitters were reviewed. The structure is based on a high-electron-mobility transistor and featured with doubly interdigitated grating gates. The dual grating gates can alternately modulate the 2D electron densities to periodically distribute the plasmonic cavities along the channel, acting as an antenna. The device can emit broadband terahertz radiation even at room temperature from self-oscillating 2D plasmons under the DC-biased conditions. When the device is subjected to laser illumination, photo-generated carriers stimulate the plasma oscillation, resulting in enhancement of the emission. We observed and characterized broadband terahertz emission from the devices fabricated in two structures: a standard single-heterostructure HEMT with metal grating gates and a DD-HEMT with semiconducting 2D electron gas grating gates. The mechanism of the self-oscillating broadband emission was examined and was interpreted as multiple modes of plasmon excitations including DC-current-driven and/or photocarrier-stimulated plasmon instability and thermally excited incoherent plasmons. Currently, maximum available emission power from a single device is of the order of 1 μW, which is comparable at 1 THz with that for an RTD oscillator but would be the highest at higher frequencies of all the electron devices. The conversion efficiency (the ratio of the output power to the consumption) is of the order of 10^{-3}, which is also the highest of all the electron devices. Further improvement on spectral narrowing and then higher efficiency is the subject. Frequency tunability by means of the gate-bias control has not yet been achieved, which is also another subject.

Acknowledgments

The authors would like to acknowledge Professor M Dyakonov at Montpellier 2 University, France, and Professor Victor Ryzhii at the University of Aizu, Japan, for many helpful discussions. They also thank Drs D Coquillat and F Teppe at GES-UMR5650, CNRS, and Montpellier 2 University, France, for their experimental support and Dr. G M Tsymbalov at the Institute of Radio Engineering and Electronics, Saratov Branch, Russia, for his theoretical support. This work was financially supported in part by the SCOPE Program from the MIC, Japan, and by the Grant in Aid for Scientific Research (S) from the JSPS, Japan. A part of this work has been carried out at the Laboratory for Nanoelectronics and Spintronics, Research Institute of Electrical Communication, in Tohoku University. One author (VVP) acknowledges support from the Russian Foundation for Basic Research (grant No 06-02-16155) and the 'Quantum nanostructures' program of the Russian Academy of Sciences. The authors from Montpellier University acknowledge the region of Languedoc-Roussillon 'Terahertz platform' as well as GDR-E 'Teraherz sources and detectors' projects.

References

[1] Tonouchi M 2007 Cutting-edge terahertz technology *Nature Photon.* **1** 97–105
[2] Hopfel R A, Vass E and Gornik E 1982 *Phys. Rev. Lett.* **49** 1667
[3] Tsui D C, Gornik E and Logan R A 1980 *Solid State Commun.* **35** 875
[4] Okisu N, Sambe Y and Kobayashi T 1986 *Appl. Phys. Lett.* **48** 776
[5] Hopfel R, Lindemann G, Gornik E, Stangl G, Gossard A C and Wiegmann W 1982 *Surf. Sci.* **113** 118
[6] Wilkinson R J *et al* 1992 Plasmon excitation and self-coupling in a bi-periodically modulated two-dimensional electron gas *J. Appl. Phys.* **71** 6049–61
[7] Hirakawa K, Yamanaka K, Grayson M and Tsui D C 1995 *Appl. Phys. Lett.* **67** 2326
[8] Dyakonov M and Shur M 1993 *Phys. Rev. Lett.* **71** 2465
[9] Knap W, Lusakowski J, Parenty T, Bollaert S, Cappy A, Popov V V and Shur M S 2004 *Appl. Phys. Lett.* **84** 2331
[10] Lusakowski J, Knap W, Dyakonova N and Varani L 2005 *J. Appl. Phys.* **97** 064307
[11] Dyakonova N, Teppe F, Lusakowski J, Knap W, Levinshtein M, Dmitriev A P, Shur M S, Bollaert S and Cappy A 2005 *J. Appl. Phys.* **97** 114313
[12] Mikhailov S A 1998 *Phys. Rev.* B **58** 1517–32
[13] Bakshi P *et al* 1999 *Appl. Phys. Lett.* **75** 1685
[14] Colombelli R, Capasso F, Gmachl C, Hutchinson A L, Sivco D L, Tredicucci A, Wanke M C, Sergent A M and Cho A Y 2001 *Appl. Phys. Lett.* **78** 2620
[15] Tredicucci A, Köhler R, Mahler L, Beere H E, Linfield E H and Ritchie D A 2005 *Semicond. Sci. Technol.* **20** S222
[16] Ryzhii V, Satou A and Shur M 2006 *IEICE Trans. Electron.* **E89-C** 1012
[17] Ryzhij V, Bannov N A and Fedirko V A 1984 *Fiz. Tekh. Poluprovodn.* **8** 769
[18] Knap W, Deng Y, Rumyantsev S and Shur M S 2002 *Appl. Phys. Lett.* **81** 4637
[19] Otsuji T, Hanabe M and Ogawara O 2004 *Appl. Phys. Lett.* **85** 2119
[20] Teppe F, Knap W, Veksler D and Shur M S 2005 *Appl. Phys. Lett.* **87** 052107
[21] El Fatimy A *et al* 2006 *Appl. Phys. Lett.* **89** 131926
[22] Otsuji T, Meziani Y M, Hanabe M, Ishibashi T, Uno T and Sano E 2006 *Appl. Phys. Lett.* **89** 263502
[23] Meziani Y M, Otsuji Y, Hanabe M, Ishibashi T, Uno T and Sano E 2007 Room temperature generation of terahertz radiation from a grating-bicoupled device: size effect *Appl. Phys. Lett.* **90** 061105
[24] Meziani Y M, Otsuji T, Hanabe M and Sano E 2007 Threshold behavior of photoinduced plasmon-resonant self-oscillation in a new interdigitated grating gates device *Japan. J. Appl. Phys.* **46** 2409–12
[25] Suemitsu T, Meziani Y M, Hosono Y, Hanabe M, Otsuji T and Sano E 2007 Novel plasmon-resonant terahertz-wave emitter using a double-decked HEMT structure *65th Device Research Conf. (DRC) Dig. (Notre Dame, IN, June 2007)* pp 157–8
[26] Otsuji T, Meziani Y M, Hanabe M, Nishimura T and Sano E 2007 Emission of terahertz radiation from InGaP/InGaAs/GaAs grating-bicoupled plasmon-resonant emitter *Solid State Electron.* **51** 1319–7
[27] Meziani Y M, Hanabe M, Otsuji T and Sano E 2008 *Phys. Status Solidi* c **5** 282
[28] Meziani Y M, Handa H, Knap W, Otsuji T, Sano E, Popov V V, Tsymbalov G M, Coquillat D and Teppe F 2008 Room temperature terahertz emission from grating coupled two-dimensional plasmons *Appl. Phys. Lett.* **92** 201108
[29] Nishimura T *et al* 2008 Broadband trahertz emission from dual-grating gate HEMTs-mechanism and emission spectral

profile *66th Device Research Conf. (DRC) Dig. (Santa Barbara, CA, June 2008)* pp 263–4
[30] Otsuji T, Hanabe M, Nishimura T and Sano E 2006 *Opt. Express* **14** 4815
[31] Hanabe M, Nishimura T, Miyamoto M, Otsuji T and Sano E 2006 Structure-sensitive design for wider tunable operation of terahertz plasmon-resonant photomixer *IEICE Trans. Electron.* **E89-C** 985–92
[32] Dyakonov M and Shur M 1996 Detection, mixing, and frequency multiplication of terahertz radiation by two-dimensional electronic fluid *IEEE Trans. Electron. Devices* **43** 380–7
[33] Hanabe M, Otsuji T, Ishibashi T, Uno T and Ryzhii V 2005 Modulation effects of photocarriers on the terahertz plasma-wave resonance in high-electron-mobility transistors under interband photoexcitation *Japan. J. Appl. Phys.* **44** 3842–7
[34] Perera A G U, Matsik S G, Liu H C, Gao M, Buchanan M, Schaff W J and Yeo W 2000 *Appl. Phys. Lett.* **77** 741
[35] Popov V V, Polischuk O V, Teperik T V, Peralta X G, Allen S J, Horing N J M and Wanke M C 2003 *J. Appl. Phys.* **94** 3556
[36] Popov V V, Tsymbalov G M and Horing N J M 2006 *J. Appl. Phys.* **99** 124303
[37] Cheremisin M V and Samsonidze G G 2006 Terahertz plasma wave generation in ultrashort-channel field effect transistors: the essential role of carrier drift velocity saturation *J. Appl. Phys.* **99** 123707
[38] Sano E 2002 Simulation of carrier transport across heterojunctions based on drift-diffusion model incorporating an effective potential *Japan. J. Appl. Phys.* **41** L1306–8
[39] Takanashi Y, Takahata K and Muramoto Y 1999 Characteristics of InAlAs/InGaAs high-electron-mobility transistors under illumination with modulated light *IEEE Trans. Electron. Devices* **46** 2271–7
[40] Shur M S and Lu J-Q 2000 Terahertz sources and detectors using two-dimensional electronic fluid in high electron-mobility transistors *IEEE Trans. Microw. Theory Tech.* **48** 750–6